



Interface characteristics between TiN and matrix and their effect on solidification structure

Tian-peng Qu¹ · De-yong Wang¹ · Hui-hua Wang¹ · Dong Hou¹ · Jun Tian¹ · Shao-yan Hu¹ · Li-juan Su¹

Received: 14 August 2020 / Revised: 19 November 2020 / Accepted: 19 November 2020 / Published online: 3 February 2021
© China Iron and Steel Research Institute Group 2021

Abstract

Heterogeneous nucleation is an effective way to promote the dispersion and precipitation of second-phase particles in steel and refine the grain size of the solidification structure. Not only refining as-cast structure grain size, but TiN in ferritic stainless steel can also pin grain boundaries and restrain the overgrowth of grains during rolling. The interface characteristics between TiN and heterogeneous phases (high-melting inclusions and ferrite phase) were studied based on the wetting angles between molten steel with different compositions and TiN substrate, and on the matching degree between TiN and ferrite lattice. It was found that, for the molten steel with the same composition, the wetting angle with the TiN substrate was significantly smaller than the contact angles with the other three substrates, while the wetting angle between ferrite phase and TiN was the smallest. The lattice matching was compared among MgAl₂O₄, TiN and δ matrix by means of a high-resolution transmission electron microscope, which revealed that a coherent or semi-coherent interface was formed between the crystal plane (400) of MgAl₂O₄ and the crystal plane (200) of TiN, as well as between the crystal plane (200) of TiN and the crystal plane (110) of δ matrix, with a lattice misfit of 5.1% and 3.4%, respectively. Finally, these two characteristics between TiN and ferrite phase were both explained from the perspective of interfacial energy. The microstructure refinement mechanism from high temperature to room temperature can be better reflected by the proposed wetting–lattice misfit theory.

Keywords TiN · Heterogeneous nucleation · Interfacial wetting · Lattice matching · Grain refinement

1 Introduction

In the process of continuous casting, increasing the ratio of equiaxed crystals has an important impact on improving the quality of rolled products [1]. At present, the control measures to improve the ratio of equiaxed crystals include low superheat casting, electromagnetic stirring (EMS), adding nucleating agent, etc. [2–5]. Adding Ti or rare earth (RE) to steel to form a heterogeneous nucleating agent based on heterogeneous nucleation mechanism can notably raise the ratio of equiaxed crystals in casting slabs, which is beneficial for reducing the internal quality defects in slabs.

TiN, which is ubiquitous in Ti-bearing steel, has a critical influence on the properties of steel and the control of grain size in the heat-affected zone during welding. On the one hand, TiN particles can be formed by adding Ti in steel to fix the element N, inhibit the growth of NbN and VN particles, and play the role of Nb and V pinning grain boundaries. On the other hand, the nucleation of δ -Fe as nucleation sites can be remarkably promoted by the TiN particles based on the good lattice matching between TiN and ferrite phase. Because of the lattice matching between TiN and ferrite, TiN is used to induce the nucleation of intragranular ferrite during welding in order to enhance the strength and toughness of welded joints [6, 7]. The studies performed by Kimura et al. [8, 9] further confirmed that the Mg–Ti interaction could significantly increase the ratio of equiaxed crystals in as-cast ferritic stainless steel. Park et al. [10] and Kim et al. [11] observed the atomic arrangement on MgAl₂O₄–TiN and TiN– δ -Fe interfaces by using a transmission electron microscope (TEM), which

✉ Hui-hua Wang
hhwang@suda.edu.cn

✉ Dong Hou
houdong0702@suda.edu.cn

¹ Shagang School of Iron and Steel, Soochow University, Suzhou 215021, Jiangsu, China

further confirmed that TiN could promote the heterogeneous nucleation of δ -Fe, while Mg-bearing particles could promote the formation of TiN. In the production of ferritic stainless steel, the addition of Ti is generally employed to refine grain size [12–14]. After adding Ti, the solidification structure is apparently refined. However, the grain size of the nucleation core TiN of ferrite is too big, which would adversely affect the surface quality of the ultra-thin-rolled products. How to obtain dispersed TiN particles with a small particle size and a high number density is of great significance to refine the high-temperature microstructure and enhance the mechanical properties of steel. Therefore, it is necessary to further refine the size of TiN particles without compromising the heterogeneous nucleation effect of TiN particles. An effective control method available now is to add Mg alloy to Ti-bearing stainless steel [15–18] for promoting the dispersion and precipitation of TiN particles with the help of micron-/nano-sized MgO or MgAl₂O₄ particles existing in high-temperature molten steel. The refinement mechanism is mainly attributed to the good lattice matching between the heterogeneous nucleation cores and the nucleation matrix, which has been widely recognized in the field of light metals metallurgy [19–22].

Although the refinement effect of Mg treatment on TiN particles can be explained by the lattice misfit theory to some extent, there has been no report on any microscale analysis of the interface characteristics among phases (MgAl₂O₄-TiN- δ) in Mg-treated Ti-bearing ferritic stainless steel. In this paper, the ferritic stainless steel SUS430 was taken as the study object, and the interface characteristics among MgAl₂O₄, TiN and the matrix in stainless steel were analyzed microscopically. Based on the interfacial energy theory, the internal mechanism of how Mg treatment improves the grain refinement of Ti-bearing stainless steel was explained, thus providing theoretical guidance for developing an innovative grain refinement technology.

2 Experimental method

The sessile droplet method was adopted in this study to measure the contact angle between molten steel and substrate. Specimens were taken from five commercial types of steels (iron) with different compositions, including commercially pure iron, steel cord, die steel, stainless steel, high-sulfur steel, etc., whose chemical compositions are listed in Table 1. Before starting the experiments, all tested steel specimens were made into $\phi 5$ mm \times 5 mm cylinders by wire cutting, and then, their surfaces were polished to remove the oxidation layer. The mass of each specimen was controlled in the range of 0.70 ± 0.02 g. The substrate

for testing was a target plate coated with 99.99% pure TiN through magnetron sputtering, of which the surface roughness was 0.1 μ m.

The instrument for measuring the contact angle in experiments was an OCA25-HTV1800 high-temperature and high-vacuum contact angle measuring device (KRUSS GmbH, Germany). This device is composed of an image acquisition system, a molybdenum disilicide resistance furnace, a rapid cooling and circulation system and a composite vacuum gauge, as shown in Fig. 1. An alundum furnace tube with an inner diameter of 40 mm and a length of 990 mm was placed horizontally at the center of the resistance furnace body, and its both ends were completely sealed by quartz covers. A high-speed camera (resolution of 2048×1088 pixels) was set to collect high-definition images of specimens. The heating and image acquisition of specimens were accurately controlled by a computer, and the real-time temperature of specimens was measured by a B-type thermocouple placed at the center of the furnace tube. During testing, high-purity argon was continuously introduced after removing the moisture and oxygen by a CYAr-4A argon gas purifier.

The contact angle measurement experiment comprised the following steps: (1) The metal specimen was placed above the inclusion substrate before testing and then pushed into the center of the furnace tube slowly by a feeding rod. The upper surface of the substrate should be maintained at the horizontal level absolutely throughout this step. (2) The furnace tube was completely sealed, and the mechanical pump was started up for air exhaust. Then, the air was exhausted continuously using a molecular pump till the pressure reached 10^{-3} Pa. At this time, the high-purity argon gas (purity of 99.999 vol.%) purified by the argon gas purifier was introduced into the furnace tube at a flow rate of 50 L/h to prevent the specimen from being oxidized. The flow balance between the inlet and the outlet gas was maintained throughout the experiment, and the high-purity argon gas in the furnace was always in circulation. (3) The heating switch was turned on to heat up the specimens to 1823 K (the commercially pure iron specimen was heated up to 1873 K due to its high melting point), ensuring completely melting the specimens. (4) When the specimen began to melt, the contact angle was observed and measured through the program ADVANCE on the computer; a video was recorded and photographs were taken until the measured contact angle did not change anymore. Then, high-definition (HD) photographs were taken for the metal droplet on the substrate, and the broken line graph of contact angle values was saved. The contours of metal droplet and substrate were accurately extracted in ADVANCE, and the appropriate fitting method was selected from those provided by the program (such as Laplace-Young and Ellipse) to measure the high-

Table 1 Chemical composition of metal specimens (wt.%)

No.	Steel type	C	Si	Mn	P	S	Cr	Ni	Cu	Al	Ti	N
1	Pure iron	0.002	0.008	0.020	0.009	0.005	< 0.020	< 0.010	< 0.030	0.030	0.020	0.0030
2	Steel cord	0.820	0.190	0.820	0.012	0.008	0.170	–	–	–	–	0.0025
3	Die steel	0.320	0.800	0.200	0.014	0.010	5.040	0.026	0.050	–	–	0.0035
4	Stainless steel	0.035	0.250	0.300	0.030	0.003	16.050	0.300	0.300	–	0.010	0.0028
5	High-sulfur steel	0.060	0.020	1.080	0.063	0.320	–	–	–	–	–	0.0036

– indicates a trace amount

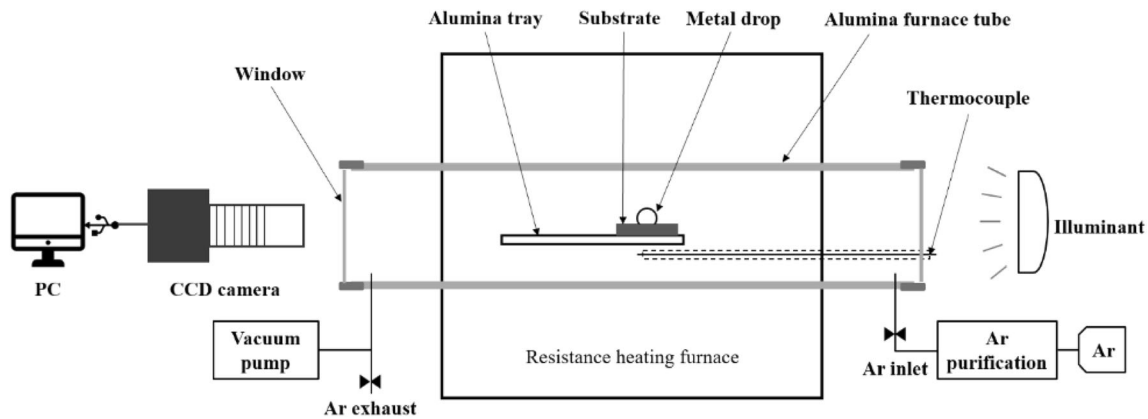


Fig. 1 Schematic diagram of high-temperature contact angle measuring device. PC Personal computer; CCD charge-coupled device

temperature contact angle. Each group of experiments was repeated three times to guarantee the reproducibility of data.

The characteristics of the interface between solidified metal and substrate were analyzed using an SU5000 scanning electron microscope (Hitachi Inc., Tokyo, Japan). Specimens were then prepared using an ion polishing system (FIB, HELIOS NanoLab 600i, FEI Inc., OR, USA) for the transmission electron microscope analysis. After that, a high-resolution TEM (HRTEM, FEI TalosF-200x, FEI Inc., OR, USA) was used to analyze the microscopic characteristics of the inclusions.

3 Results and discussion

3.1 Analysis of interfacial wettability

In the process of high-temperature contact angle measurement, the contact angle between metal droplet and substrate changed with the temperature and time, mainly because the wetting was a dynamic process. The contact angle corresponding to the saturated wetting was called saturated contact angle, on which numerous researches have been done [23–31]. In order to assure the consistency of the test conditions, the temperature was held at 1823 K

to measure the contact angle between the metal droplet and substrate after the contact angle no longer fluctuated. It should be noted that the contact angles measured in this experiment were all apparent ones because chemical reactions inevitably occurred on the interface between metal droplet and substrate. In the case of the contact angle greater than 120° (super non-wetting), it has been reported that the Laplace–Young fitting method has the highest accuracy in measuring the contact angle between phases [32]. In the case of the contact angle ranging from 90° to 120° (non-wetting) and the case of the contact angle less than 90° , the Ellipse fitting has the highest measurement accuracy.

The photographs of the five types of metal droplets spreading out on the TiN substrate surface and the measured values of left and right contact angles are shown in Fig. 2 (the displayed values were measured after the contact angle no longer changed, that is, the saturated contact angle values). It can be found that due to the slight vibration of the furnace body when heating up or the slight sloping of the sample platform, the substrate was hard to be maintained at the horizontal level absolutely, resulting in a slight deviation between the measured left (L) and the right (R) contact angles. Therefore, in the follow-up calculations, the average value of the left and right contact angles

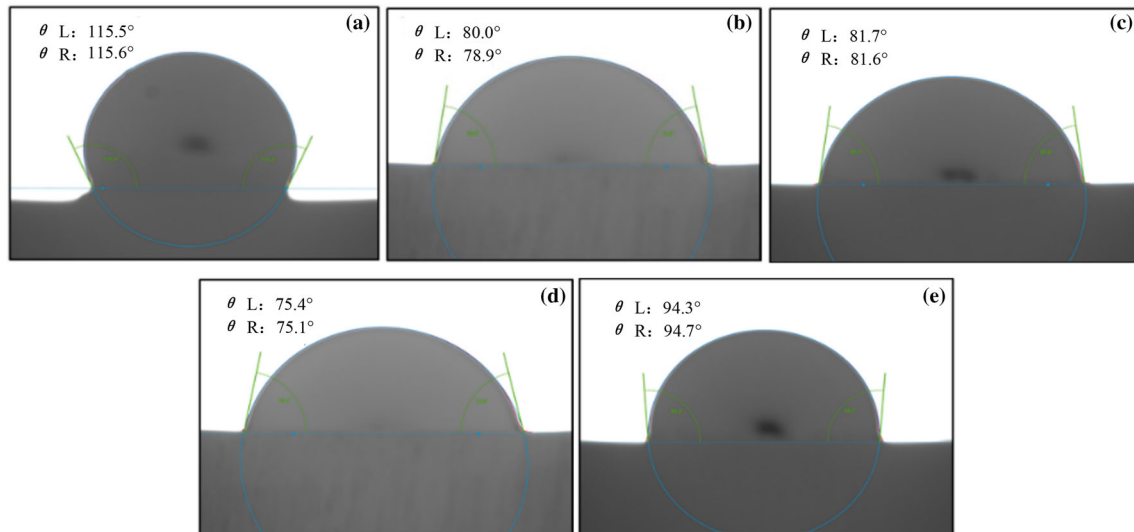


Fig. 2 Photographs of high-temperature contact angle θ between metal droplet and TiN substrate. **a** Pure iron; **b** steel cord; **c** die steel; **d** stainless steel; **e** high-sulfur steel

was selected as the apparent contact angle obtained from each group of experiments.

The changes in the contact angle of each metal droplet on the TiN substrate surface are illustrated in Fig. 3. As can be seen, the contact angle of the pure iron droplet on the TiN substrate changes little over the holding time. There was no chemical reaction between the pure iron droplet and the TiN substrate, and simply the physical wetting occurred. The pure iron droplet has the largest wetting angle (115.55°) among the others. The contact angles of the other metal droplets on the TiN substrate show all downtrends and tend to be flat at last, which is primarily due to the chemical reaction between them and the TiN substrate. When reaching an equilibrium state (the curve turns flat), the measured is a saturated contact angle, which can reflect the wetting and the interfacial tension between the metal droplet and the TiN substrate.

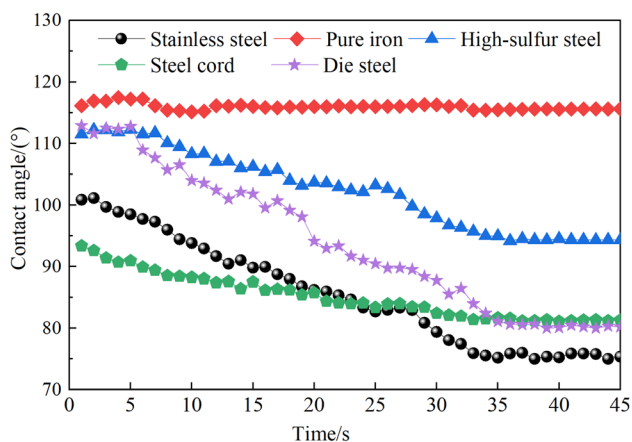


Fig. 3 Changes in contact angle between metal droplet and TiN substrate

In an authors' previous study [32], the high-temperature contact angles between the five types of metal droplets and the Al_2O_3 , MgO and MgAl_2O_4 substrates were measured, thus obtaining three sets of values, which were compared with the values of TiN substrate in this paper. Figure 4 shows the broken line graphs of contact angles between the five types of steel (iron) droplets and the Al_2O_3 , MgO , MgAl_2O_4 and TiN substrates. As can be seen, the contact angles between the metal droplets and the Al_2O_3 , MgO and MgAl_2O_4 substrates are all greater than 90° , indicating that the substrates are not wetted with the droplets. The contact angles with the TiN substrate indicate that there is non-wetting for the pure iron and the high-sulfur steel, but wetting for the steel cord, the die steel and the stainless steel (with contact angles $< 90^\circ$), among which the ferritic stainless steel has the optimal wettability with the TiN

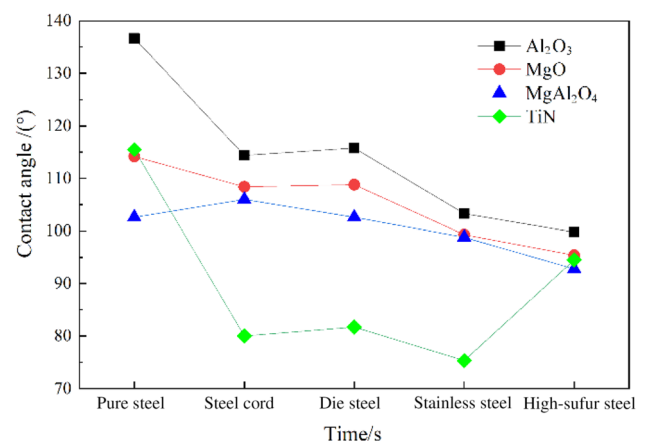


Fig. 4 Contact angles between different liquid phases and Al_2O_3 , MgO , MgAl_2O_4 and TiN substrates [32]

substrate. For each type of metal droplet, the inclusions are always ranked in terms of their non-wettability as follows: $\text{Al}_2\text{O}_3 > \text{MgO} > \text{MgAl}_2\text{O}_4$. Their difference in non-wettability is the most obvious for the molten pure iron and is the least for the molten stainless steel, while the TiN substrate exhibits the best wettability.

The TiN substrate has the best wettability with the ferritic stainless steel. The specimens were cut apart longitudinally to observe and analyze microscopically their wetting sections using a field emission scanning electron microscope, of which the results are shown in Fig. 5. As can be seen, the part above the interface is the stainless steel matrix and the part below it is the TiN substrate, accompanied by an approximately 10- μm -wide transition region between them, which positively influenced their interfacial wetting characteristics.

3.2 Analysis of lattice matching characteristics on interface

By adding Mg and Ti alloys to the molten ferritic stainless steel, TiN inclusion particles were extracted from Mg-bearing ferritic stainless steel specimens based on the FIB-HRTEM technique. The TEM scanning results are shown in Fig. 6. As can be seen, the particle size is approximately

3.5 μm , and an obvious three-layer structure is detected. The core of these particles is MgAl_2O_4 composed of Mg, Al and O, and what is located in the middle is the TiN layer, covered by (Ti, Nb)C outermost. It can be inferred based on the three-layer structure that the three substances have the following precipitation order in the process of solidification: the MgAl_2O_4 is precipitated first, next is the TiN, and then the TiC/NbC. The phase precipitated earlier can be used as the heterogeneous nucleation site for the phase precipitated later, and their lattice matching relationship should be investigated for the heterogeneous nucleation ability.

Figure 7 shows the diffraction spots of the core MgAl_2O_4 , the middle TiN layer and the δ matrix, in which the MgAl_2O_4 has a similar lattice structure with the TiN (both are cubic structures), but the matrix δ -Fe has a rectangular structure. Since both the MgAl_2O_4 and the TiN belong to the face-centered cubic structure of NaCl type, the crystal plane (100) is the close-packed plane of atoms, whereas the δ matrix is arrayed in a body-centered cubic structure, and its close-packed plane of atoms is the crystal plane (110). The lattice constants of MgAl_2O_4 , TiN and δ matrix determined by the diffraction spots are 0.80812, 0.42553 and 0.28569 nm, respectively. The comparison between every two overlapped diffraction spots is

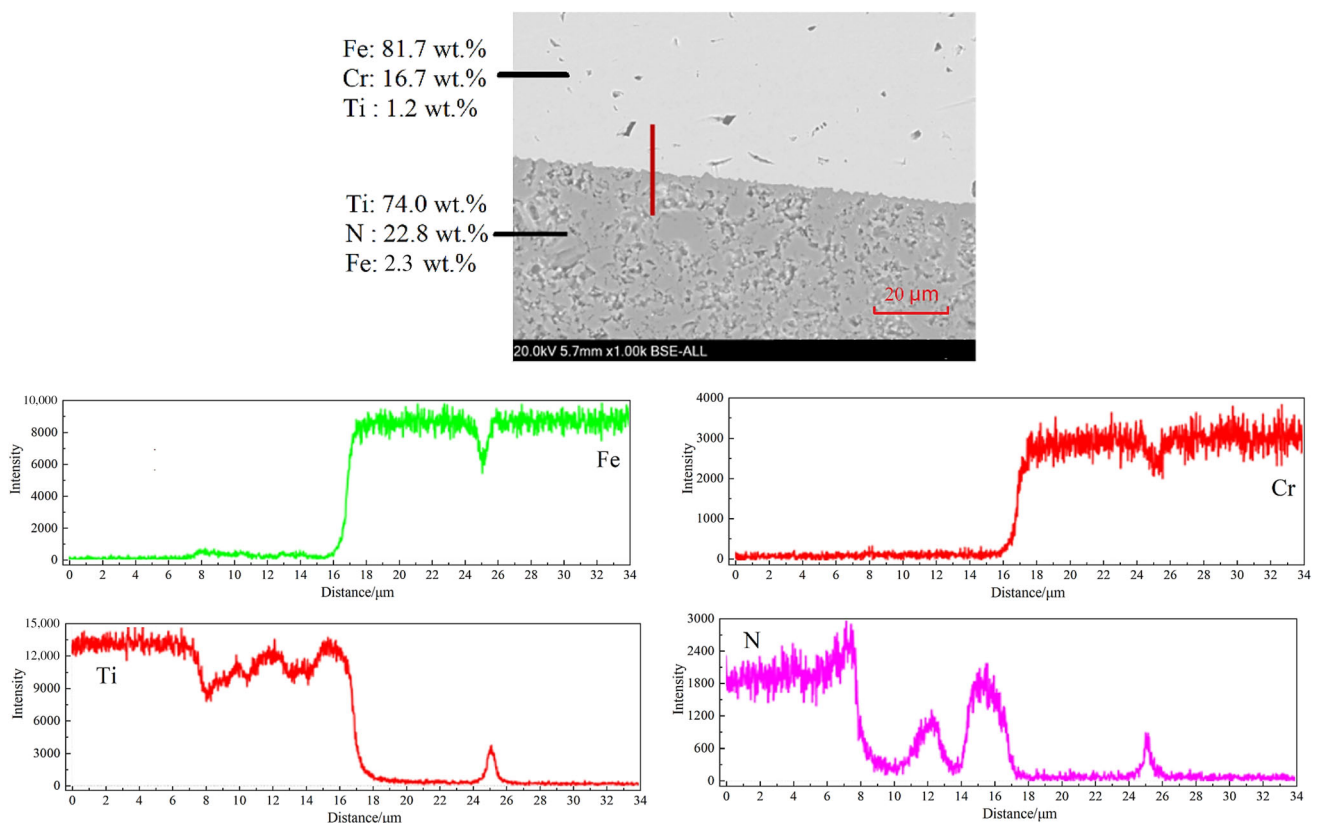


Fig. 5 Line scanning results of elements on interface between stainless steel and TiN

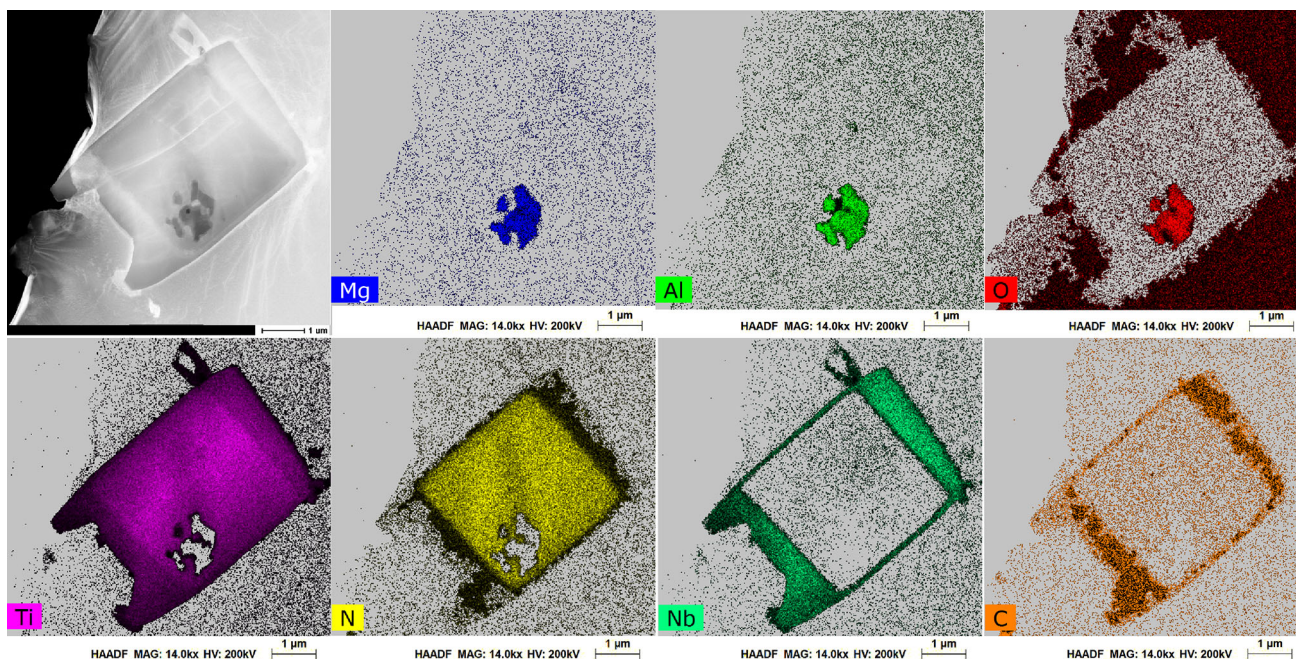


Fig. 6 TEM and EDS images of duplex TiN particles in ferritic stainless steel

exhibited in Fig. 8, where the position with enhanced brightness represents the entire overlapping of diffraction spots between the two phases. Figure 8a illustrates that the crystal plane (400) of MgAl_2O_4 well overlaps with the crystal plane (200) of TiN, that is, $(400)_{\text{MgAl}_2\text{O}_4} // (200)_{\text{TiN}}$. The lattice misfit between the two phases is calculated to be 5.1%, proving a good coherent relationship between them. Figure 8b shows the overlapping image of diffraction spots between TiN and δ matrix, where the crystal plane (200) of TiN basically overlaps with the crystal plane (110) of δ matrix, which means that the $(200)_{\text{TiN}}$ can be well matched with the $(110)_{\delta\text{-Fe}}$, with a lattice misfit of 3.4%. Therefore, a good lattice matching is also confirmed between TiN and the matrix $\delta\text{-Fe}$ for a certain crystal phase.

3.3 Analysis based on interfacial energy theory

There are generally two nucleation modes in the initial stage of solidification for molten ferritic steel: homogeneous nucleation and heterogeneous nucleation. Due to numerous deoxidation products with complex compositions and varied sizes existing in molten steel, such as Al_2O_3 , MgAl_2O_4 and MgO , some nonmetallic inclusion particles with appropriate sizes and high melting points can become the nucleation sites for high-temperature δ -ferrite and reduce the nucleation undercooling of $\delta\text{-Fe}$. It is assumed that the $\delta\text{-Fe}$ nucleates on the surface of inclusion plate, as shown in Fig. 9. During stable nucleation, the

relationship among liquid phase (molten steel), δ phase crystal nucleus and inclusion is as follows:

$$\sigma_{\text{IL}} = \sigma_{\text{ID}} + \sigma_{\text{LD}} \cos \theta \quad (1)$$

Theoretically, the heterogeneous nucleation frequency is expressed as follows:

$$I = I_0 \exp(-\Delta G^*/(kT)) \quad (2)$$

where

$$I_0 = (nkT/h) \exp(-\Delta G_a/(kT)) \quad (3)$$

$$\Delta G^* = (16\pi/3) [\sigma_{\text{LD}}^3 f(\theta) / \Delta G^2] \quad (4)$$

$$f(\theta) = \frac{2 - 3 \cos \theta + \cos^3 \theta}{4} \quad (5)$$

I is the nucleation frequency of $\delta\text{-Fe}$; n is the number density of nucleation sites; k is the Boltzmann constant; h is the Planck constant; T is the absolute temperature; ΔG_a is the critical activation energy of nucleation of an atom; ΔG^* is the Gibbs free energy; ΔG is the nucleation driving force; and $f(\theta)$ is the contact angle factor.

Whether the high-melting nonmetallic inclusions in high-temperature molten steel promote the nucleation of high-temperature δ -ferrite depends on $f(\theta)$ identified in Eq. (5) and θ , whose relationship is indicated by the curve in Fig. 10. With the decrease in θ , that is, the wettability between the new phase and the bonded phase getting better, $f(\theta)$ decreases, and the nucleation frequency of the new phase derived from Eqs. (2) and (4) also increases significantly. The contact angle shown in Fig. 10 must be small enough for the purpose of promoting the induced

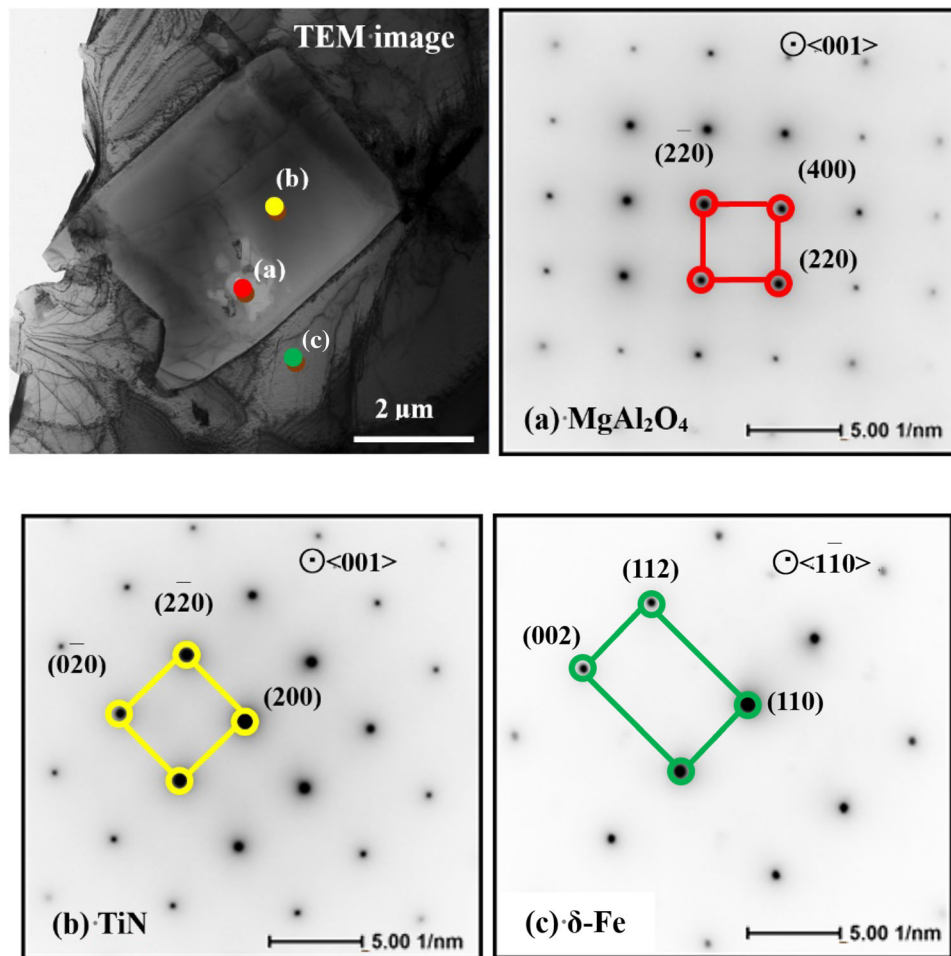


Fig. 7 Selected area electron diffraction (SAED) patterns of MgAl_2O_4 , TiN and $\delta\text{-Fe}$ in steel

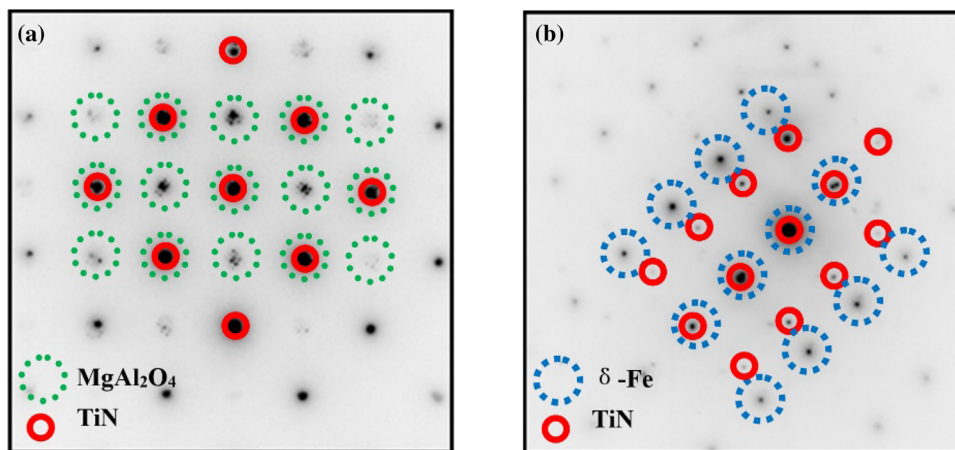


Fig. 8 Overlapped SAED pattern between adjacent phases. **a** MgAl_2O_4 /TiN; **b** TiN/ $\delta\text{-Fe}$

nucleation effect of high-melting inclusions on the high-temperature δ -ferrite. That is, σ_{ID} in Eq. (1) shall be minimized. By this way, the critical undercooling required for the nucleation of $\delta\text{-Fe}$ is reduced, thus accelerating the

nucleation of $\delta\text{-Fe}$ in the initial stage of solidification. The contact angle at the three-phase interface (molten steel– $\delta\text{-Fe}$ inclusions) can be obtained using a direct or indirect method, and it is reasonable and effective to verify the

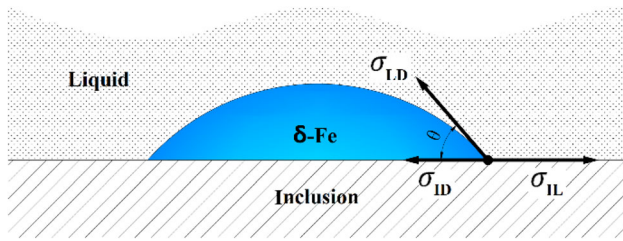


Fig. 9 Schematic diagram of heterogeneous nucleation of δ phase on inclusion surface

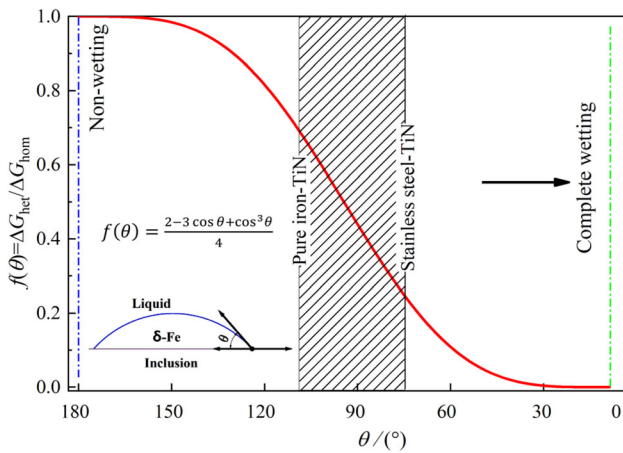


Fig. 10 Variation curve of contact angle factor

effectiveness of a nucleating agent by means of the interfacial wetting behavior.

The matching problem between phases in the process of solid-state phase transformation is well explained by the lattice matching theory [33], but it is unable to obtain the lattice matching state in the high-temperature region, which lacks evidentiary support. Moreover, with regard to the nucleation of the first-layer atoms in a liquid phase on the surface of solid particles in the initial stage of steel solidification (the atomic stacking model is shown in Fig. 11), the bonding behavior of the atoms in a liquid phase (in long-range ordering) with the atoms in a solid phase (in short-range ordering) is not applicable to the

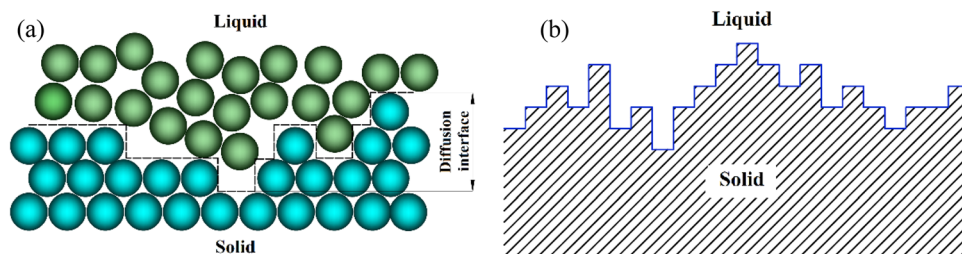


Fig. 11 Atomic stacking model and schematic diagram of solid–liquid interface. **a** Atomic stacking model; **b** schematic diagram of diffusion interface

lattice matching theory, and more attention shall be paid to the wetting behavior of molten steel on the surface of solid particles. Therefore, the integrated theory of interfacial wetting–lattice misfit was considered in this paper to be more suitable for describing the nucleation process of high-temperature liquid phase and the nucleation process of solid-state phase transformation.

3.4 Refinement effect of solidification structure

The authors have preliminarily explored the Mg–Ti synergistic treatment for the ferritic stainless steel 430 in a previous experimental study [34]. Water-cooled specimens were extracted from a molten bath using a quartz bucket before and after magnesium addition and then corroded to obtain the solidification structure as exhibited in Fig. 12. The solidification structure before Mg treatment contained columnar crystals and equiaxed crystals (the ratio of equiaxed crystals was about 37%, and the average grain size in the central equiaxed crystal zone was about 79 μm). After adding Ni–Mg alloy to the molten bath, the solidification structure of the water-cooled specimens was refined notably, with the columnar crystal zone shrinking sharply (the ratio of equiaxed crystals reaching 64%).

TiN is the main factor to refine the grains of ferritic stainless steel. As mentioned above, the macrograins were refined after adding Mg to the steel, and TiN particles were formed in the solid–liquid coexisting zone because of the deoxidation product MgO or MgAl_2O_4 in molten steel. In the process of solidification and cooling of molten steel, MgO or MgAl_2O_4 particles could act as heterogeneous nucleation cores for TiN particles to promote the dispersion and precipitation of TiN particles, as shown in Fig. 13. As a result of the good interfacial bonding between high melting oxides and TiN particles, TiN particles were bonded to the oxides for massive nucleation at the beginning of nucleation, thus increasing the TiN nucleation density. Furthermore, based on the desirable interface bonding between TiN and δ -Fe, a large number of dispersed TiN particles provided plentiful sites for the nucleation of δ -Fe in the initial stage of solidification to

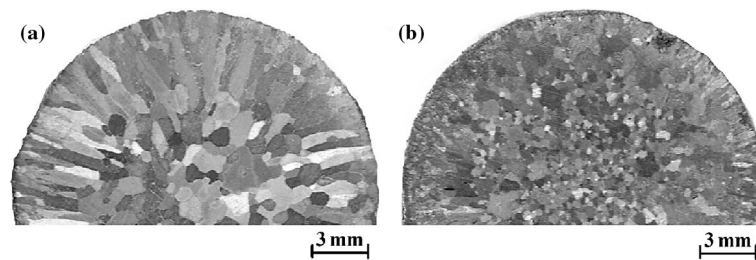


Fig. 12 Comparison of solidification microstructure of water-cooled specimens before (a) and after (b) magnesium addition

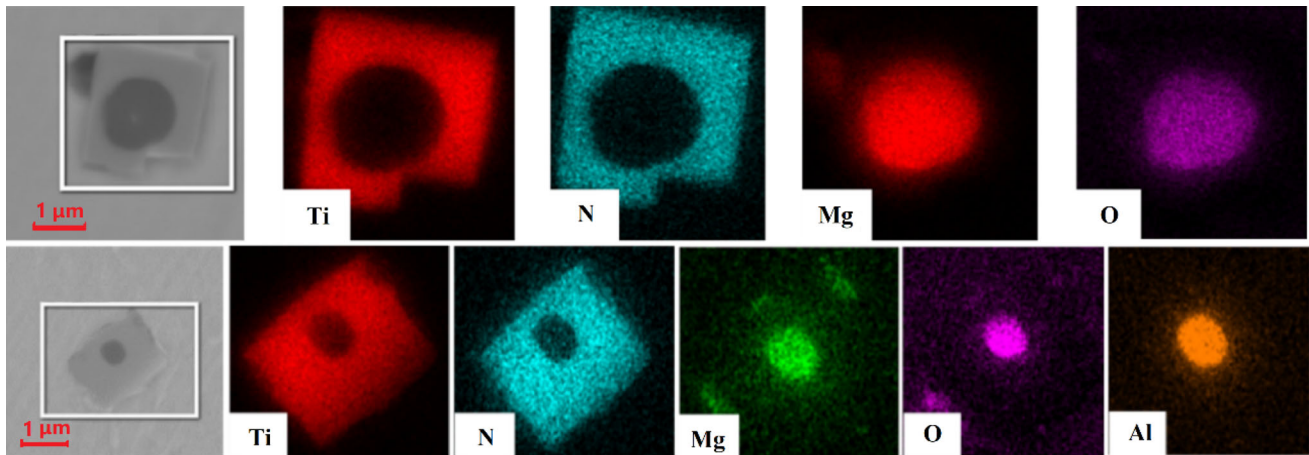


Fig. 13 Appearance of TiN particles in specimens after magnesium treatment

finally obtain fine grains and thus refine the solidification structure.

4 Conclusions

1. How the TiN particles induce the nucleation of ferrite in the initial stage of solidification can be reflected by the interfacial wetting characteristics. For the molten steel with the same composition, its wetting angle with the TiN substrate was significantly smaller than its contact angles with the other three substrates, while the wetting angle between the ferrite phase and TiN was the smallest.
2. The FIB-HRTEM analysis results revealed that a coherent or semi-coherent interface was formed between the crystal plane (400) of MgAl_2O_4 and the crystal plane (200) of TiN, as well as between the crystal plane (200) of TiN and the crystal plane (110) of δ matrix, with a lattice misfit of 5.1% and 3.4%, respectively.
3. Based on the good lattice matching, the MgAl_2O_4 particles formed from the Mg added in the ferritic stainless steel provided heterogeneous nucleation sites for TiN and then the TiN particles provided heterogeneous nucleation sites for δ matrix. The dispersed

MgAl_2O_4 particles initially formed by Mg treatment promoted the remarkable refinement of macrograins eventually. After Mg treatment, the average grain size in the central equiaxed crystal region of specimens decreased from 79 to 34 μm .

4. The interfacial wetting characteristics between high-temperature molten steel and TiN, as well as the lattice matching characteristics between room temperature matrix and TiN, can be explained from the perspective of interfacial energy. This unified wetting–lattice misfit theory may provide a theoretical support for developing new heterogeneous nucleating agents.

Acknowledgements This work is supported by the National Natural Science Foundation of China (Grant Nos. 51774208, 52074186, 51804205 and U1860205).

References

- [1] T. Maki, *Tetsu-to-Hagane* 81 (1995) N547–N555.
- [2] A. Suzuki, *Tetsu-to-Hagane* 60 (1974) 774–783.
- [3] Y. Ujiie, H. Maede, Y. Itoh, S. Ogibayashi, H. Seki, K. Wada, Y. Itoh, *Tetsu-to-Hagane* 67 (1981) 1297–1306.
- [4] T. Ohashi, T. Hiromoto, H. Fujii, Y. Nuri, K. Asano, *Tetsu-to-Hagane* 62 (1976) 614–623.
- [5] J.S. Park, J.H. Park, *Steel Res. Int.* 85 (2014) 1303–1309.

- [6] Y. Morikage, K. Oi, F. Kawabata, K. Amano, *Tetsu-to-Hagane* 84 (1998) 510–515.
- [7] D.S. Sarma, A.V. Karasev, P.G. Jonsson, *ISIJ Int.* 49 (2009) 1063–1074.
- [8] K. Kimura, S. Fukumoto, G.I. Shigesato, A. Takahashi, *ISIJ Int.* 53 (2013) 2167–2175.
- [9] S. Fukumoto, K. Kimura, A. Takahashi, *Tetsu-to-Hagane* 98 (2012) 351–357.
- [10] J.S. Park, D.H. Kim, J.H. Park, *J. Alloy. Compd.* 695 (2017) 476–481.
- [11] J.Y. Kim, N.R. Oh, Y.H. Oh, Y.T. Cho, W.B. Lee, S.K. Kim, H.U. Hong, *Mater. Charact.* 132 (2017) 348–353.
- [12] J.S. Park, C. Lee, J.H. Park, *Metall. Mater. Trans. B* 43 (2012) 1550–1564.
- [13] J.P. Liang, C.J. Song, L.X. Wang, Z.J. Li, Q.J. Zhai, *Mater. Technol.* 27 (2012) 333–336.
- [14] Y.M. Tian, Z.P. Chen, Y.T. Xu, M.T. Gong, D. Shu, *J. Iron Steel Res.* 26 (2014) No. 6, 61–66.
- [15] K. Isobe, *ISIJ Int.* 50 (2010) 1972–1980.
- [16] H. Mizukami, M. Numata, A. Yamanaka, *ISIJ Int.* 56 (2016) 1420–1426.
- [17] H. Ohta, H. Suito, *ISIJ Int.* 47 (2007) 197–206.
- [18] D.Y. Wang, M.F. Jiang, H. Matsuura, F. Tsukihashi, *Steel Res. Int.* 85 (2014) 16–25.
- [19] Y. Watanabe, H. Sato, *J. Jpn. I. Met. Mater.* 64 (2014) 157–163.
- [20] M. Li, J.M. Li, D. Qiu, Q. Zheng, G. Wang, M.X. Zhang, *Philos. Mag.* 96 (2016) 1556–1578.
- [21] L. Wang, L. Yang, D. Zhang, M. Xia, Y. Wang, J.G. Li, *Metall. Mater. Trans. A* 47 (2016) 5012–5022.
- [22] L. Wang, W.Q. Lu, Q.D. Hu, M.X. Xia, Y. Wang, J.G. Li, *Acta Mater.* 139 (2017) 75–85.
- [23] B.J. Monaghan, M.W. Chapman, S.A. Nightingale, *ISIJ Int.* 50 (2010) 1707–1712.
- [24] C. Xuan, H. Shibata, S. Sukenaga, P.G. Jonsson, K. Nakajima, *ISIJ Int.* 55 (2015) 1882–1890.
- [25] J.F. Padday, D.R. Russell, *J. Colloid Sci.* 15 (1960) 503–511.
- [26] B.F. Dyson, *Trans. Metall. Soc. AIME* 227 (1963) 1098–1103.
- [27] L.J. Zhou, Z.H. Pan, W.L. Wang, J.Y. Chen, L.W. Xue, T.S. Zhang, L. Zhang, *Metall. Mater. Trans. B* 51 (2020) 85–94.
- [28] M. Shin, J. Lee, J.H. Park, *ISIJ Int.* 48 (2008) 1665–1669.
- [29] W.L. Wang, E.Z. Gao, L.J. Zhou, L. Zhang, H. Li, *J. Iron Steel Res. Int.* 26 (2019) 355–364.
- [30] L.J. Zhou, L.J. Wen, W.L. Wang, Il. Sohn, *Metall. Mater. Trans. B* 48 (2017) 1943–1950.
- [31] W.L. Wang, J.W. Li, L.J. Zhou, J. Yang, *Met. Mater. Int.* 22 (2016) 700–706.
- [32] K.L. Chen, D.Y. Wang, D. Hou, T.P. Qu, J. Tian, H.H. Wang, *ISIJ Int.* 59 (2019) 1735–1743.
- [33] B.L. Bramfitt, *Metall. Trans. B* 1 (1970) 1987–1995.
- [34] C.W. Zhang, T.P. Qu, D.Y. Wang, J. Tian, D. Hou, *J. Iron Steel Res.* 31 (2019) 661–667.